Active Control for Turbulent Drag Reduction by Periodic Blowing and Suction

Ching-Te Lin *
California Institute of Technology, Pasadena, CA 91125, USA.

Andres Goza †
University of Illinois at Urbana-Champaign, Urbana, IL 61801, USA.

H. Jane Bae ‡
California Institute of Technology, Pasadena, CA 91125, USA.

This study examines the effects of spatially and temporally periodic blowing and suction on turbulent drag and coherent structures in channel flow. We first determine the minimal domain necessary for consistent analysis of the impact of harmonic blowing and suction. We then conduct a systematic exploration of wavenumber and frequency domains for spanwise-constant standing and traveling waves under small wall-transpiration velocity amplitudes to identify parameters that lead to drag increase or decrease. Our findings indicate that optimal parameters result in a 2.93% drag reduction for standing waves and a 3.62% drag reduction for traveling waves. Turbulent kinetic energy (TKE) analysis shows that drag reduction is closely linked to TKE reduction in the near-wall region above the blowing section, whereas drag increase occurs when TKE reduction in the blowing section is offset by TKE increase in the suction section. Furthermore, two-point velocity correlation analysis reveals a consistent enhancement of streamwise rolls in drag-reducing scenarios, with streamwise streaks inclined toward the wall. In contrast, drag-increasing scenarios exhibit attenuation of these coherent structures, with streamwise streaks inclined away from the wall.

I. Introduction

Turbulent drag significantly impacts the energy efficiency of fluid machinery and aircraft. For instance, approximately half of the energy consumption of commercial aircraft is due to turbulent drag from the boundary layer [1]. Similarly, in industrial fluid transportation spanning thousands of kilometers for water, petroleum, and natural gas, turbulent drag within pipes represents a substantial portion of energy use. Therefore, even marginal reductions in drag for these systems could lead to significant savings in energy and operational costs. Skin friction drag, as a major component of turbulent drag, is a primary focus for drag reduction strategies. For practical reasons, the majority of studies focus on altering drag properties of the flow by actuating at the wall. Surface geometry changes (e.g., riblets or prescribed surface motion), blowing and suction, or passively adaptive wall motion via compliant structures (possibly involving complex structures such as metamaterials), all fall within this category of wall actuation. This study adopts harmonic blowing and suction to mitigate skin friction drag in turbulent channel flow. In addition to its direct relevance to, e.g., synthetic jet wall actuation, this approach is expected to indicate promising mechanisms to be harnessed for drag reduction by the other wall-based actuation strategies mentioned.

Methods for reducing skin friction or drag can be categorized as passive or active approaches. Passive techniques modify flow or surface characteristics without requiring additional energy input [2]. Notably, surface-mounted longitudinal grooves (riblets) have shown success in reducing turbulent boundary layer drag despite increasing surface area. Initial observations by Walsh and Weinstein [3] reported consistent drag reductions of up to 8% with riblets, a finding corroborated by subsequent numerical studies [4–6] elucidating their disruption of near-wall shear layers. More recent work by Endrikat et al. [7] optimized riblet shapes with considerations to mitigate the Kelvin-Helmholtz instability. Permeable substrates present another passive option for turbulent flow control, explored by Breugem et al. [8]

---

*Graduate Student, Department of Mechanical and Civil Engineering, Student Member AIAA
†Assistant Professor, Department of Aerospace Engineering, Senior Member AIAA
‡Assistant Professor, Graduate Aerospace Laboratories, Senior Member AIAA

and further studied under various conditions such as two-side permeable walls [9] and anisotropic permeable substrates [10, 11].

Active control techniques, while requiring energy input, often achieve greater drag reduction. These techniques primarily include feedback control and spanwise wall oscillation, both of which modify the boundary condition on the wall. Choi et al. [12] demonstrated that opposition control, using a blowing/suction boundary condition to counteract wall-normal velocity at a specific distance from the wall, can reduce drag by up to 30%. This method creates a "virtual" wall in the near-wall region, effectively lifting the near-wall cycle and reducing drag [13–15]. Bewley et al. [16] utilized optimal control, a predictive strategy, achieving flow relaminarization and a 50% drag reduction. Spanwise wall oscillation, first introduced by Jung et al. [17], resulted in a 40% drag reduction, with subsequent studies refining the optimal oscillating frequencies and Reynolds number dependencies [18–21]. Quadrio et al. [22] reported that only a specific speed of forward-traveling wall oscillation effectively reduces drag. Yao and Hussain [23] further explored drag reduction in supersonic turbulent flow through spanwise wall oscillation. These studies highlight the potential of wall modifications for drag reduction and provide mechanistic insights that guide implementation.

In this study, we conduct a detailed parametric investigation of another active drag reduction approach: harmonic blowing and suction. Quadrio et al. [24] applied a streamwise-varying blowing suction boundary condition on turbulent channel flow, observing a 13% drag reduction. Gómez et al. [25] analyzed the impact of wall transpiration on turbulent pipe flow using resolvent analysis and dynamic mode decomposition, identifying a reorganization of coherent structures in the controlled flow. Moarref and Jovanović [26] and Lieu et al. [27] applied receptivity analysis to the linearized Navier-Stokes equation of a channel flow to study the control effect of streamwise-traveling harmonic blowing and suction, validating theoretical results with direct numerical simulation (DNS) at low Reynolds numbers. Cheng et al. [28] experimentally investigated periodic blowing via streamwise slits, achieving a maximum drag reduction of 70% with an open-loop approach and 23% with a closed-loop approach. Despite these findings, optimal combinations of parameters such as spatial wavenumber, temporal frequency, and actuator amplitude remain to be determined. This study seeks to address these open questions through a comprehensive parametric study.

The aim is to expand the understanding of the drag reduction effects of periodic blowing and suction, examining the frequencies, wavenumber, and amplitude of the periodic forcing on the wall. This parametric study will elucidate the contribution of each parameter, paving the way for advanced control schemes in channel flow based on critical parameters. We perform a series of DNS under spanwise-constant harmonic blowing and suction boundary conditions on the channel walls. The periodic blowing and suction are applied in two distinct forms: a standing waveform, where the sinusoidal wave oscillates at a given temporal frequency and streamwise-traveling waveform, coupling streamwise and temporal frequencies. The primary focus is on small velocity amplitude actuations, of the order of the friction velocity. While previous research has shown significant drag reduction with larger amplitudes, our study prioritizes small amplitude control due to its feasibility [11, 24, 28]. Small amplitude oscillations can potentially be achieved using novel surface materials [29] and may be actuated through passive rather than active control.

The paper is organized as follows. In Section II, the blowing and suction actuation, flow configuration, and simulation details are described. In Section III, we discuss the effect of domain-size under periodic blowing suction. In Section IV, the effect on drag of standing and traveling waves are assessed in detail. A discussion regarding the effects of actuation on TKE and key coherent structures is provided as well. Lastly, the conclusion is given in the Section V.

II. Methodology

A. Harmonic Forcing

We first define the blowing and suction wall boundary conditions for the two types of periodic forcing studied in this paper: standing and traveling waves. First, the standing waveform (type I forcing) is given by

$$V_w^{\mathrm{I}}(x, z, t; A, k_x, k_z, \omega) = A \cos(k_x x) \cos(k_z z) \cos(\omega t), \tag{1}$$

where V_w is the wall-normal velocity at the wall, and A, k_x, k_z and ω are the amplitude, streamwise wavenumber, spanwise wavenumber, and temporal frequency, respectively. Second, the streamwise traveling waveform (type II forcing) is given by

$$V_w^{\mathrm{II}}(x, z, t; A, k_x, k_z, \omega) = A \cos(k_x x - \omega t) \cos(k_z z) \cos(-\omega t). \tag{2}$$

Note that in Eq. (2), the wave of the wall-normal velocity travels in the streamwise direction with the phase speed $c = \omega/k_x$.

2
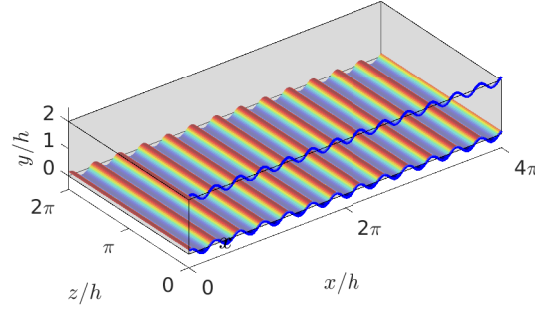
Fig. 1 Schematic of the computational domain and blowing and suction boundary condition.

Quadrio et al. [24] investigated the effect of streamwsie-periodic wall transpiration, which is equivalent to the type I forcing with $k_z = 0$ and $\omega = 0$. The current work extends this work and systematically studies the parameter space (A, k_x, k_z, ω) with $\omega \neq 0$ for type I forcing to identify the effect on turbulent drag. In addition, type II forcing is investigated to complete the parametric study. In this study, the waves are limited to spanwise constant forcing ($k_z = 0$).

We quantify the effect on turbulent drag as the net change in the time-averaged wall-shear stress τ_w,

$$\%\Delta\tau_w = 100\frac{\langle\tau_{w,c}\rangle - \langle\tau_{w,o}\rangle}{\langle\tau_{w,o}\rangle}, \tag{3}$$

where the subscripts c and o represent quantities evaluated for the controlled and reference (unactuated) flow, respectively, and $\langle\cdot\rangle$ denotes the time-averaged quantities after the transient response. A negative value of $\%\Delta\tau_w$ represents drag reduction, and a positive value represents drag increase.

B. Numerical Setup

A series of DNS are performed to evaluate the control performance of harmonic blowing and suction in a wall-bounded turbulent flow. The simulations are computed by solving the incompressible Navier-Stokes equations at a friction Reynolds number $Re_\tau = u_\tau h/\nu \approx 180$, where u_τ is the friction velocity, h represents channel half-height, and ν is the kinematic viscosity. Periodic boundary conditions are applied at the streamwise and spanwise boundaries. The boundary conditions on both walls are enforced by no slip conditions in the wall-parallel directions and transpiration given by Eqs. (1) or (2) in the wall-normal direction.

The computational domain (illustrated in the Fig. 1) is defined with streamwise and spanwise lengths of $L_x/h = 4\pi$ and $L_z/h = 2\pi$, respectively. This domain size is determined through a series of numerical experiments detailed in Section III, which confirms that the minimal domain size required to study the effect of blowing and suction on the wall-shear stress is given by $(L_x/h, L_z/h) = (4\pi, 2\pi)$. Grid resolutions in the homogeneous direction are uniform with $\Delta x^+ \approx 9.97$ and $\Delta z^+ \approx 4.98$, where the superscript + denotes the wall units defined by ν and u_τ. For the wall-normal direction, the grid is stretched using a hyperbolic tangent function such that Δy^+ varies from a minimum of 0.16 near the wall to a maximum of 7.34 at the channel center. The simulations utilize a staggered, second-order finite difference scheme [30] in space.

The time-marching scheme is given by the fractional-step method [31] with a third-order Runge–Kutta integration [32]. A fixed time step of $\Delta t^+ \approx 0.01$ is applied, and the total integration time is $T^+ \approx 3000$ to mitigate transient effects from additional periodic forcing. Code validation is achieved in prior studies of turbulent channel flow [33–35].

III. Domain-Size Study and Validation

The minimal computational domain with harmonic forcing on the walls is first investigated to minimize the computational cost and validate the statistical convergence of several important quantities. In the case of no wall transpiration, the minimal flow unit [36] provides the minimal domain size in which the flow is turbulent and the low-order turbulence statistics are in good agreement with experiments in the near-wall region. The size of the minimal

3
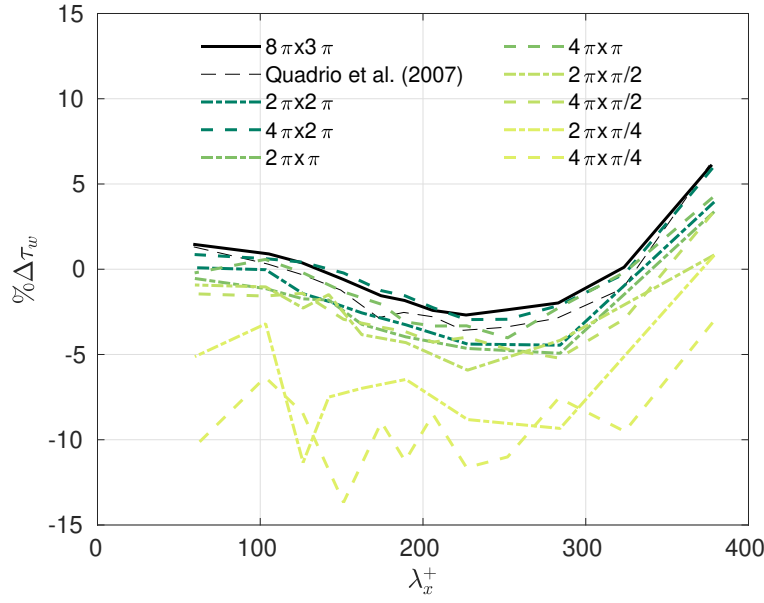
Fig. 2 Change in wall-shear stress, $\%\Delta\tau_w$, for different streamwise forcing wavelength λ_x^+. Line type denotes the streamwise domain size and line color represents the spanwise domain size. Reference cases are given by Quadrio et al. [24] (black dashed line) and the largest computational domain $(L_x/h, L_z/h) = (8\pi, 3\pi)$ (solid black line).

| L_x/h ⟍ L_z/h	$\pi/4$	$\pi/2$	π	2π
2π	11.64	3.16	2.96	2.49
4π	12.99	3.18	1.63	0.57

Table 1 The maximum relative error (%) of mean shear stress with respect to the largest domain $(L_x/h, L_z/h) = (8\pi, 3\pi)$.

flow unit is $L_z^+ \approx 100$ (or $L_z/h \approx \pi/4$ for $Re_\tau \approx 180$) such that the domain contains a single low-velocity streak, consisting of a longitudinal strip on which a thin layer of spanwise vorticity is lifted away from the wall. In the case of wall roughness, Chung et al. [37] found that the minimal span not only needs to satisfy the original constraint of natural wall-bounded turbulence but must also be constrained by the roughness height h_r. The minimal flow unit for riblets, for example, should be wide enough to fully immerse the roughness elements, which leads to the constraint of $L_z > h_r/0.4$, and long enough to capture the largest streamwise characteristic scale. In the present study, we observe that, much like flow over rough surfaces, additional constraints should also be applied to the wall-bounded turbulence under harmonic blowing and suction.

To investigate the domain-size effect of harmonic forcing on the walls, we use a streamwise periodic blowing and suction given by

$$V_w(x; A, k_x) = V_w^{\mathrm{I}}(x; A, k_x, k_z = 0, \omega = 0), \tag{4}$$

where $A^+ = 0.7$ and $\lambda_x^+ = 2\pi/k_x^+$ ranges from 59 to 377. The results are shown in Fig. 2 and Table 1, where we observe that a domain size greater than the minimal flow unit [36] of $L_z/h \approx \pi/4$ is necessary to converge to the statistics given by Quadrio et al. [24] and our DNS results from a large domain, $(L_x/h, L_z/h) = (8\pi, 3\pi)$. In particular, in Table 1, we show the maximum relative error, which is defined as $100(\langle\tau_w\rangle - \langle\tau_{w,8\pi\times3\pi}\rangle)/\langle\tau_{w,8\pi\times3\pi}\rangle$, for each computational domain size, where $\langle\tau_{w,8\pi\times3\pi}\rangle$ is the mean shear stress obtained from a DNS of the large domain. The data indicates that when the domain size is increased to $(L_x/h, L_z/h) = (4\pi, 2\pi)$, the maximum error significantly decreases to below 1%. Consequently, in the present study, domain size of $(L_x/h, L_z/h) = (4\pi, 2\pi)$ will be used for the remainder of the results.

4
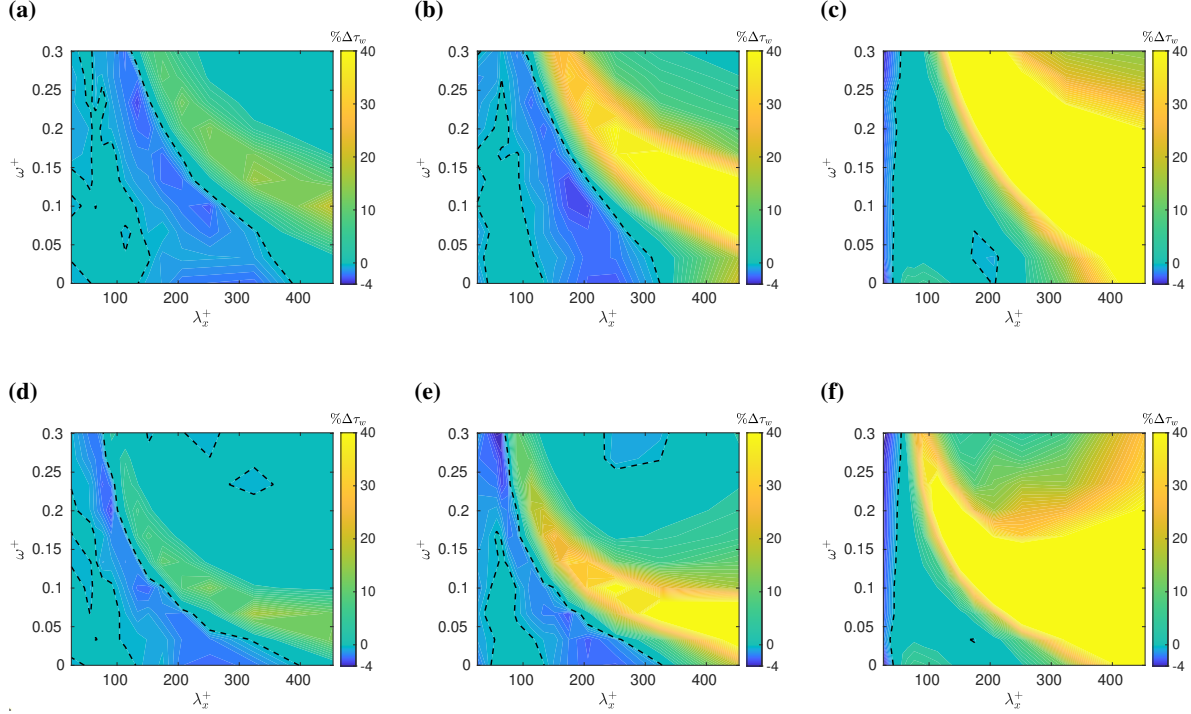
Fig. 3   Change in wall-shear stress for type I forcing with (a) $A^+ = 0.35$**, (b)** $A^+ = 0.7$**, and (c)** $A^+ = 1.4$ **and type II forcing with (d)** $A^+ = 0.35$ **(e)** $A^+ = 0.7$**, and (f)** $A^+ = 1.4$**. Dashed lines indicate** $\%\Delta\tau_w = 0$

IV. Results and Discussion

In this section, the effect on turbulent drag achieved via spanwise-constant standing and traveling waveforms is analyzed using first- and second-order statistics. To avoid transient effects, $\Delta\tau_w$ is calculated after $t^+ = 500$ and averaged over $\Delta t^+ = 2500$ to ensure statistical stationarity. We first study the change in wall-shear stress for the range of parameters studied in the section IV.A. We then identify changes in TKE and the two-point velocity correlation in section IV.B and IV.C.

A. Change in wall-shear stress

The change in turbulent drag under various velocity amplitudes and forcing profiles are shown in Fig. 3. In Fig. 3 (a–c), the change in wall-shear stress for type I forcing is shown with respect to λ_x and ω for three different values of A. The contour plots reveal a drag reduction region ranging from $\lambda_x^+ \approx 150$ to $\lambda_x^+ \approx 300$ with $\omega^+ = 0$. As the frequency ω increases, we observe that the range of λ_x that exhibits drag reduction is shifted to lower wavelengths and is reduced. There is also a secondary drag reduction region at low values of λ_x for all ω that is enhanced with increasing A. We also observe that as we increase the velocity amplitude, the magnitude of $\Delta\tau_w$ in drag reduction region first increases (from $A^+ = 0.35$ to $A^+ = 0.7$) then decreases (from $A^+ = 0.7$ to $A^+ = 1.4$). For $A^+ = 1.4$, the original drag reduction region retains a similar shape but is significantly reduced in magnitude. Overall, within the range of parameters studied here, a maximum drag reduction of $\%\Delta\tau_w = -2.9$ can be achieved by a standing wave with $(\lambda_x^+, \omega^+, A^+) = (206, 0.1, 0.7)$.

On the other hand, in Fig.3 (d–f), type II forcing shows a similar drag reduction region, resulting in a 3.62% drag reduction for high-frequency oscillation $\omega^+ = 0.3$, $\lambda_x^+ = 56.7$ at $A^+ = 0.7$. Similar to the cases of type I forcing, we observe a strong drag increase region for moderate values of wavelength and frequency. However, compared to type I forcing, the size of drag increase region is reduced, and the drag increase effect diminishes faster with increasing λ_x and ω. Consequently, we observe an isolated region around $(\lambda_x^+, \omega^+) = (252, 0.3)$ that produces a slight drag reduction effect.

We note that the absolute value of drag reduction observed in the current study is significantly lower than those reported in the literature due to the limitation on the velocity amplitudes studied. However, if we consider the

5
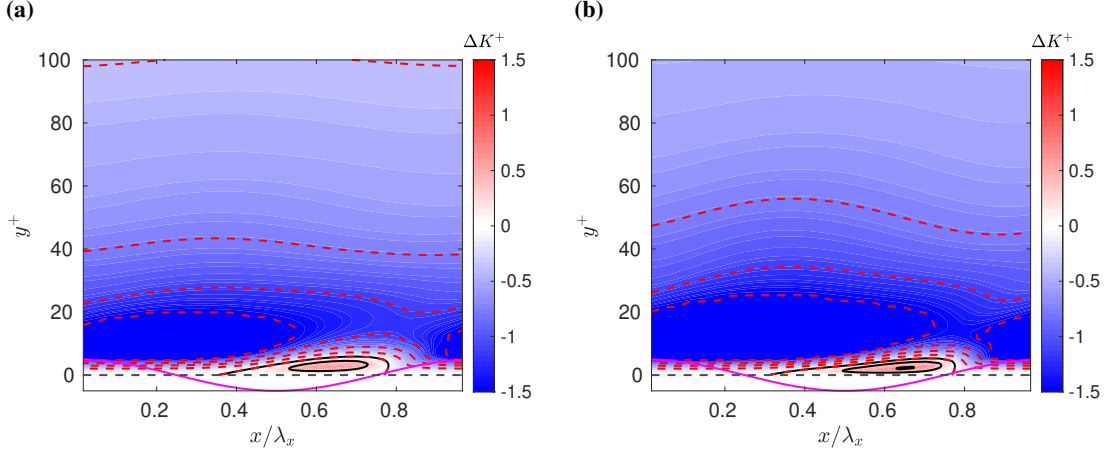
Fig. 4 Contours of phase-averaged TKE for type I forcing with (a) $(A^+, \lambda_x^+, \omega^+)$=(0.7, 251.98, , 0) and (b) $(A^+, \lambda_x^+, \omega^+)$=(1.4, 251.98, 0). Red dash lines denote the contours of negative TKE difference with the spacing of 0.3 while the black lines denote the contours of positive TKE difference with the spacing of 0.3. The magenta line represents the shape of the surface wall-normal velocity profile.

time-averaged kinetic energy input per unit area,

$$K_{in}^+ = \frac{1}{TL_xL_z} \int_0^T \int_0^{L_z} \int_0^{L_x} \frac{V_w^2}{u_\tau^2} dx dz dt, \tag{5}$$

the optimal drag reduction of %$\Delta\tau_w = -2.9$ reported in this paper is achieved with $K_{in}^+ = 0.12$, which is relatively higher than the 13% drag reduction for type I forcing with $K_{in}^+ = 5.5$ in Quadrio et al. [24] (approximately 4.5 times drag reduction with 45 times energy input) and a drag reduction of 70% with $K_{in}^+ = 6.3$ in Cheng et al. [28] (24 times drag reduction with 50 times energy input). When limited to smaller amplitudes, Quadrio et al. [24] also reported maximum drag reduction of 3.7% at $K_{in}^+ = 0.12$, similar to our observations. In the current study, the purpose of targeting the relatively small amplitude is to explore the drag reduction effect under small perturbations that are realizable by low-power actuators. The result of small perturbation control could provide a pathway to several actuator designs, including purely passive techniques involving metamaterials [29]. Even with the limitation to small amplitudes, both standing and traveling waveforms demonstrate a potential for drag reduction, with the traveling wave achieving a slightly higher maximum reduction.

B. Turbulent kinetic energy

To investigate the drag reduction mechanism of blowing and suction actuation, we compute the TKE under various phases of blowing and suction. The difference in TKE between the controlled flow and the reference flow is considered to highlight the effect of wall transpiration in the near-wall region. This TKE difference is defined as

$$\Delta K^+ = \frac{1}{2} \frac{\langle u_i' u_i' \rangle_c - \langle u_i' u_i' \rangle_o}{u_\tau^2}, \tag{6}$$

where u_i' denotes the fluctuating velocity component in the i direction. For time-varying flow, the fluctuating component u_i' is computed based on a (phase averaged) time-varying mean profile.

For standing waves, three cases are considered to compare the control effect of wall transpiration regarding the optimal time-invariant condition ($\omega = 0$), the time-varying condition ($\omega \neq 0$), and a drag increase scenario. First, for the optimal time-invariant case, the parameters of frequency and wavelength are chosen as $(\lambda_x^+, \omega^+) = (251.98, 0)$. Two types of velocity amplitudes are examined in this section. The case of $A^+ = 0.7$ and $A^+ = 1.4$ is displayed in Fig. 4. Since the blowing and suction boundary conditions of both cases are streamwise-periodic, the flow is homogeneous not only in the spanwise direction but also in the phase of the streamwise direction with period λ_x. Consequently, the

6
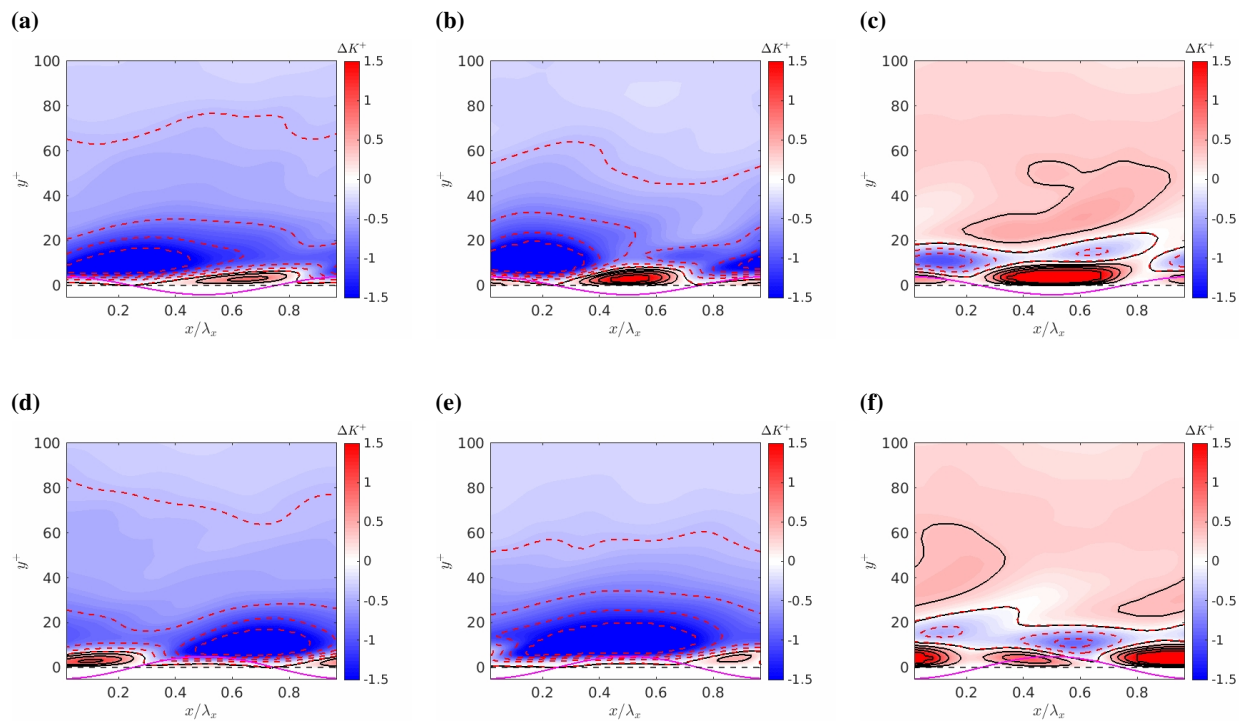
Fig. 5   Contours of phase-averaged TKE for type I forcing with (a,d) $(A^+, \lambda_x^+, \omega^+) = (0.7, 174.45, 0.13)$**, (b,e)** $(A^+, \lambda_x^+, \omega^+) = (1.4, 174.45, 0.13)$**, and (c,f)** $(A^+, \lambda_x^+, \omega^+) = (0.7, 174.45, 0.27)$ **at (a-c)** $\omega t = 0.2\pi$ **and (d-f)** $\omega t = \pi$**. Red dash lines denote the contours of negative TKE difference with the spacing of 0.3 while the black lines denote the contours of positive TKE difference with the spacing of 0.3. The magenta line represents the shape of the surface wall-normal velocity profile.**
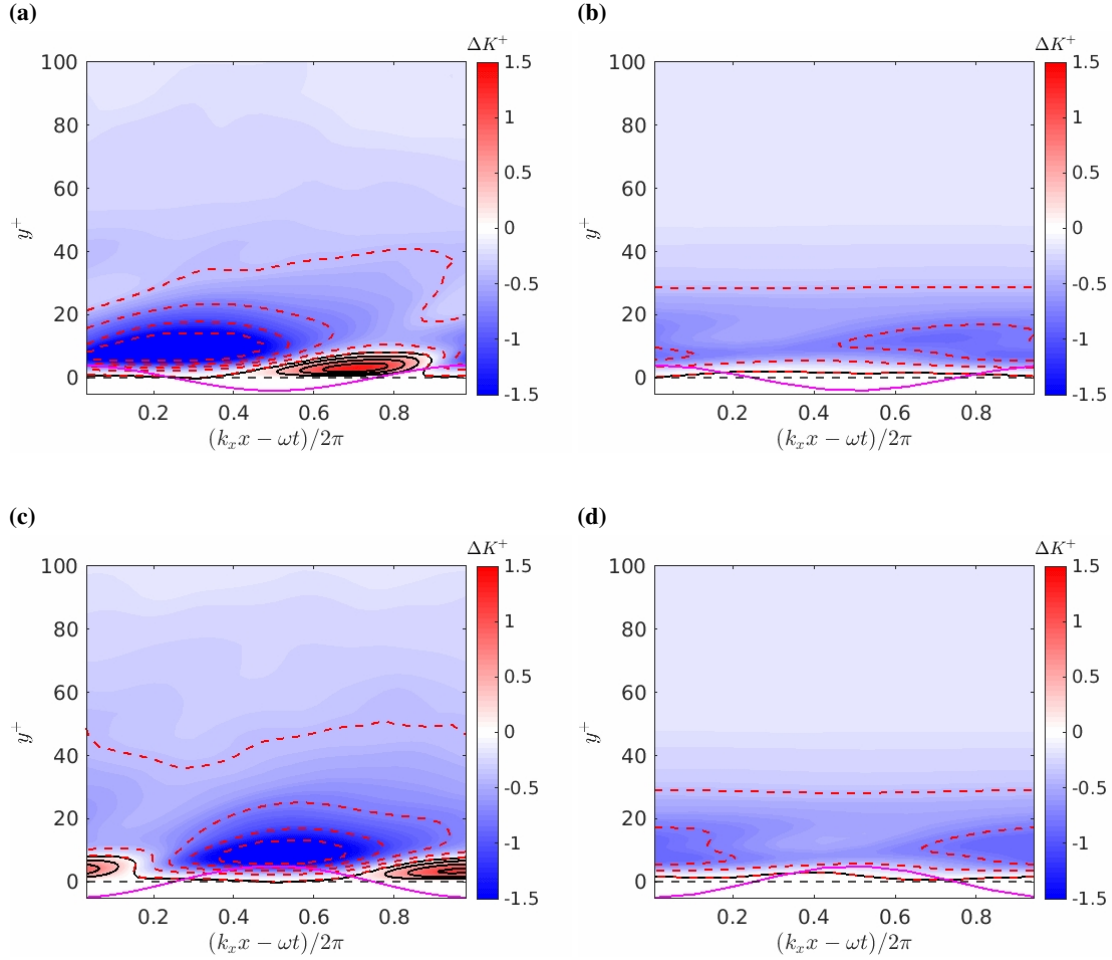
Fig. 6 **Contours of phase-averaged TKE for type II forcing with (a,c)** $(A^+, \lambda_x^+, \omega^+) = (0.7, 174.45, 0.07)$ **and (b,d)** $(A^+, \lambda_x^+, \omega^+) = (0.7, 56.7, 0.3)$ **at (a,b)** $\omega t = 0.2\pi$ **and (c,d)** $\omega t = \pi$. **Red dash lines denote the contours of negative TKE difference with the spacing of 0.3 while the black lines denote the contours of positive TKE difference with the spacing of 0.3. The magenta line represents the shape of the surface wall-normal velocity profile.**
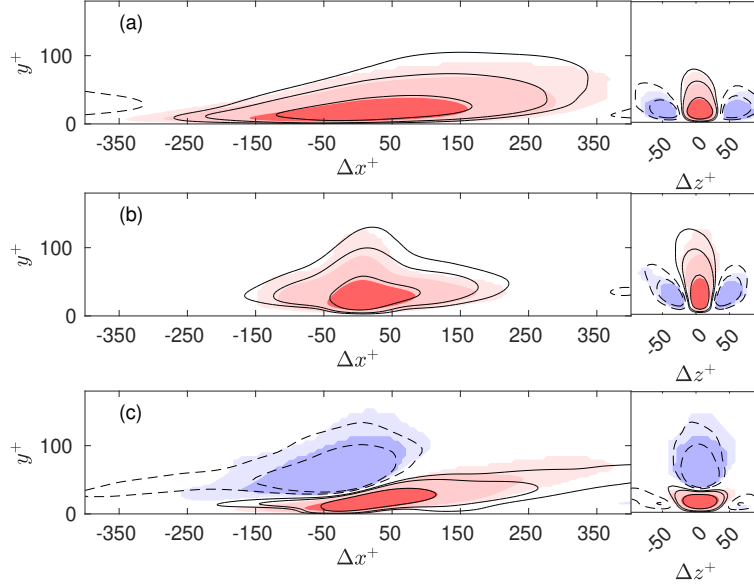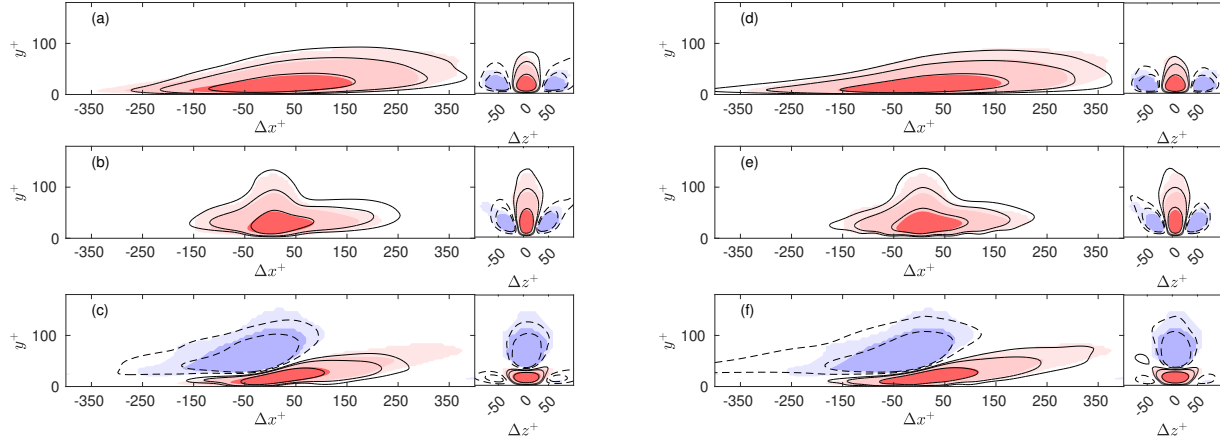
Fig. 7 Contours of (a) streamwise, (b) wall-normal, and (c) spanwise velocity auto-correlation about $y_{\text{ref}}^+ = 15$ for $(A^+, \lambda_x^+, \omega^+)=(0.7, 251.98, 0)$. Color contours indicate C_{ii} of the reference flow for positive (blue) and negative (red) correlation. Line contours indicate those of the controlled case for positive (solid) and negative (dashed) correlation. Contour levels are $C_{ii} = [-0.1, -0.05, 0.05, 0.1, 0.3]$.

TKE difference ΔK^+ is plotted as a function of the wall-normal direction and the streamwise phase, x/λ_x. In both cases, the TKE shows a significant decrease in the near-wall region coinciding with the blowing section and an increase in the suction region. This correspondence suggests that drag reduction might be achieved by creating a region of TKE decrease in the viscous sublayer and buffer layer. With increasing velocity amplitude, the drag reduction effect diminishes, as shown in the contour plot in Fig. 3. This difference is consistent with the larger region of increasing TKE in Fig. 4(b).

In Fig. 5, the optimal time-varying case $((\lambda_x^+, \omega^+) = (174.45, 0.13))$ for two different A and the drag increase case $((\lambda_x^+, \omega^+) = (174.45, 0.27))$ are compared. In these cases, since the blowing and suction condition is oscillating in time, the temporal phase-averaged technique is used to study the effect of various phases of blowing and suction conditions. We display two temporal phases, $\omega t = 0.2\pi$ and $\omega t = \pi$. As the suction and blowing sections change in time, we observe the regions associated with increase and decrease in TKE also change as well with the negative ΔK region always following the blowing section. This phenomenon can also be observed with an even more pronounced TKE increase region in the case of large amplitude, $A^+ = 1.4$. In the case of drag increase, even though there is a small region of TKE reduction above the blowing section, the TKE reduction region is lifted farther away from the wall, creating a smaller TKE increase region closer to the wall. This additional TKE increase region results in a net TKE increase, leading to over 40% drag increase.

Conversely, the reduction in turbulent fluctuations under the influence of a streamwise-traveling wave demonstrates an overall suppression for the case of high-frequency oscillations. We show the results of the traveling wave in Fig. 6, where the TKE difference is averaged not only temporally with respect to the phase but also spatially with the traveling wave. We show results for optimal cases with parameters $(A^+, \lambda_x^+, \omega^+) = (0.7, 174.45, 0.07)$ and $(A^+, \lambda_x^+, \omega^+) = (0.7, 56.7, 0.3)$. The former case is suboptimal case with the parameters of moderate streamwise wavenumber and frequency, which is close to the optimal case of standing wave. The latter is the optimal case with the maximum drag reduction of 3.62%. By comparison between two cases, high frequency oscillation of traveling wave alleviates the increase in TKE throughout the inner layer. In both temporal phases, $\omega t = 0.2\pi$ and π, the turbulent fluctuation is alleviated across the inner layer and even within the suction section. This phenomenon explains the fact that the high-frequency oscillation of the traveling wave can lead to the optimal drag reduction effect.

9

Fig. 8 **Contours of (a,d) streamwise, (b,e) wall-normal, and (c,f) spanwise velocity auto-correlation about $y_{\text{ref}}^+ = 15$ for (a–c) $(A^+, \lambda_x^+, \omega^+)=(0.7, 174.45, 0.13)$ and (d–f) $(A^+, \lambda_x^+, \omega^+)=(0.7, 56.7, 0.3)$. Color contours indicate C_{ii} of the reference flow for positive (blue) and negative (red) correlation. Line contours indicate those of the controlled case for positive (solid) and negative (dashed) correlation. Contour levels are $C_{ii} = [-0.1, -0.05, 0.05, 0.1, 0.3]$.**
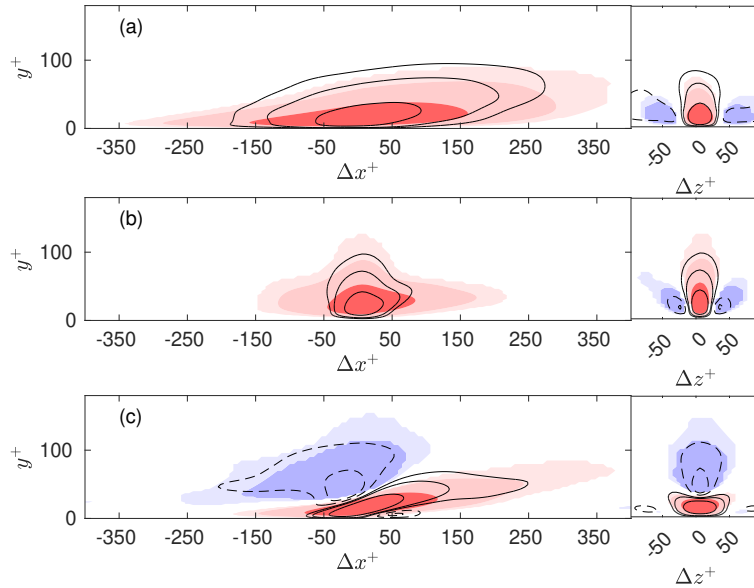
Fig. 9 **Contours of (a) streamwise, (b) wall-normal, and (c) spanwise velocity auto-correlation about $y_{\text{ref}}^+ = 15$ for $(A^+, \lambda_x^+, \omega^+)=(0.7, 174.45, 0.27)$. Color contours indicate C_{ii} of the reference flow for positive (blue) and negative (red) correlation. Line contours indicate those of the controlled case for positive (solid) and negative (dashed) correlation. Contour levels are $C_{ii} = [-0.1, -0.05, 0.05, 0.1, 0.3]$.**

10

C. Two-point velocity correlation

Analysis of the two-point velocity correlation is conducted here to investigate the change of coherent structure with the additional wall transpiration effect. Jiménez [38] demonstrated several examples regarding the identification of coherent structure in wall-bounded flow. The two-point velocity correlation is defined for a channel flow as

$$C_{ij}(\Delta_x, \Delta_z, y; y_{\text{ref}}) = \frac{\langle u_i'(x, y, z) u_j'(x + \Delta_x, y_{\text{ref}}, z + \Delta_z) \rangle}{\langle u_i'(x, y, z) u_j'(x, y_{\text{ref}}, z) \rangle}, \tag{7}$$

where u_i' is the turbulent velocity fluctuation. Due to the homogeneity in streamwise and spanwise direction and the stationarity, the correlation function C_{ij} for a channel flow is a four-dimensional function with parameters of $\Delta_x, \Delta_z, y, y_{\text{ref}}$. The reference wall-normal location is fixed at $y_{\text{ref}}^+ = 15$ in order to study coherent structures in the near-wall region related to the peak of the near-wall turbulent kinetic energy. Therefore, in the following discussion, the cross section of the three-dimensional correlation function will be displayed to study the coherent structure. In this study, the three autocorrelations of velocity fluctuation, C_{11}, C_{22}, and C_{33}, are analyzed to provide a comprehensive view of the modifications in coherent structures. Note again that the fluctuations u_i' are computed such that the temporal-phase-averaged flow field is removed.

In Fig. 7, the optimal constant blowing and suction case is illustrated to study the control effect. The Δx–y cross section of the streamwise velocity autocorrelation, C_{11}, show a slightly shortened streamwise streak due to wall transpiration. On the other hand, the spanwise rolls, indicated by C_{22} and C_{33}, is slightly elongated in the streamwise direction for the controlled flow, with the most visible differences in the spanwise velocity autocorrelation. In Fig. 7(c), both the positive and negative correlation regions are stretched in the streamwise direction compared to the base flow, with additional negative correlation regions showing up in the spanwise direction. Still, the spacing of the rolls in the spanwise direction remain largly unchanged. This stability in the spanwise direction suggests that the streamwise-periodic wall-transpiration specifically targets streamwise modifications while preserving spanwise coherence.

A similar trend can also be observed in the optimal time-varying case of standing and traveling waves. In Fig. 8(a–c), the optimal time-varying case is shown. The streamwise velocity correlation C_{11} is slightly reduced in the streamwise direction and the correlation of spanwise and wall-normal velocity stretched in the streamwise direction and remains similar in the Δz–y cross section, with the exception of the negative correlation regions of C_{33}. However, the elongation of the streamwise rolls in the streamwise direction is not as significant as the optimal time-invariant case of standing wave displayed in Fig. 8(d–f). The correlation of spanwise velocity is stretched as the time-invariant case, implying the control effect on the roller is consistent. Furthermore, streamwise streaks in the optimal controlled case demonstrate a structure slighly inclined toward the wall. This phenomenon is more significant in the time varying case. In Fig. 8(a) and (d), the streamwise streak shown in the plane of Δx–y attached to the wall compared to the uncontrolled case in both optimal cases of standing wave and traveling wave.

While the mechanisms for drag reduction via wall-transpiration differ slightly among various waveforms, the overall enhancement of coherent structures in turbulence is consistently observed. The opposite can be observed in the drag increase case illustrated in Fig. 9. In Fig. 9, all three velocity correlation functions, particularly the streamwise and spanwise components, are significantly compressed compared to the reference flow. In addtion, the streamwise streaks become siginificantly inclined away from the wall. The region of positive wall-normal correlation, which remains largely unaltered in the drag reduction case, is also reduced. A closer examination of the Δz–y plane for C_{22} and C_{33} reveals even more significant changes, indicating a decrease in streamwise rolls in the spanwise and wall-normal directions. This reduction in the size of the coherent structures, such as streamwise streaks and rolls, can be attributed to the disruption of the near-wall self-sustaining process within the turbulence.

V. Conclusion

This study investigates the effects of spanwise-constant periodic blowing and suction on drag reduction and coherent structure modifications in turbulent channel flows. A domain-size study was first conducted to validate the statistics convergence of key quantities, such as mean shear stress, under minimal computational domains. It was found that, under the circumstance of periodic blowing and suction, the minimal channel requires a spanwise length $L_z/h \gtrsim 4\pi$ to achieve statistical convergence, revealing that additional computational constraints are necessary for turbulence under harmonic blowing and suction.

The results demonstrate that optimal control parameters for both standing and traveling waves can significantly reduce drag. For standing waves, a maximum drag reduction of 2.9% was achieved with parameters

11

$(A^+, \lambda_x^+, \omega^+)$=(0.7, 174.45, 0.13), while traveling waves showed a maximum drag reduction of 3.62% with $(A^+, \lambda_x^+, \omega^+) =$ (0.7, 56.7, 0.3). We observed that the drag reduction mechanism is closely associated with modifications in TKE and the structure of turbulence. Harmonic blowing and suction is able to create significant TKE decreases in the near-wall region, particularly in the viscous sublayer and buffer layer above the blowing region, leading to drag reduction. However, as the velocity amplitude increases, the drag reduction effect diminishes due to the expansion of TKE increase regions. Temporal phase analysis for time-varying cases indicated that the dynamic switching of suction and blowing sections affects TKE distribution. Two-point velocity correlation analysis provided insights into coherent structure modifications. The optimal constant blowing and suction case showed that streamwise streaks are mitigated, and spanwise rollers are elongated, enhancing coherent structures. Similar trends were observed in the optimal time-varying cases for standing and traveling waves, although the changes were less pronounced compared to the time-invariant case. Moreover, the streamwise streaks are inclined toward the wall in the drag reduction time-varying case of both standing and traveling wave.

In conclusion, while the mechanisms for drag reduction via wall-transpiration vary slightly among different waveforms, the overall enhancement of coherent structures in turbulence is consistently observed. The drag increase case further supports this hypothesis, demonstrating significant compression of velocity correlation functions and a reduction in coherent structures. These findings underscore the importance of tailored control strategies in optimizing flow characteristics and achieving efficient drag reduction in turbulent channel flows. Future work will focus on exploring the various blowing and suction configuration, including the wide-known riblet shape, as well as the employed the optimal wavenumber and frequencies identified in this study on the feedback control design.

Acknowledgments

References

[1] Kornilov, V., "Combined Blowing/Suction Flow Control on Low-Speed Airfoils," *Flow, Turbulence and Combustion*, Vol. 106, 2021. https://doi.org/10.1007/s10494-020-00157-7.

[2] Bushnell, D. M., and McGinley, C. B., "Turbulence control in wall flows," *Annual Review of Fluid Mechanics*, Vol. 21, No. 1, 1989, pp. 1–20. https://doi.org/https://doi.org/10.1146/annurev.fl.21.010189.000245.

[3] Walsh, M., and Weinstein, L., "Drag and heat transfer on surfaces with small longitudinal fins," *11th Fluid and PlasmaDynamics Conference*, 1978, p. 1161.

[4] Choi, H., Moin, P., and Kim, J., "Direct numerical simulation of turbulent flow over riblets," *Journal of Fluid Mechanics*, Vol. 255, 1993, p. 503–539. https://doi.org/10.1017/S0022112093002575.

[5] García-Mayoral, R., and Jiménez, J., "Drag reduction by riblets," *Philosophical Transactions of the Royal Society A: Mathematical, Physical and Engineering Sciences*, Vol. 369, No. 1940, 2011, pp. 1412–1427. https://doi.org/10.1098/rsta.2010.0359.

[6] Liu, K. N., Christodoulou, C., Riccius, O., and Joseph, D. D., "Drag reduction in pipes lined with riblets," *AIAA Journal*, Vol. 28, No. 10, 1990, pp. 1697–1698. https://doi.org/10.2514/3.10459.

[7] Endrikat, S., Modesti, D., García-Mayoral, R., Hutchins, N., and Chung, D., "Influence of riblet shapes on the occurrence of Kelvin–Helmholtz rollers," *Journal of Fluid Mechanics*, Vol. 913, 2021, p. A37. https://doi.org/10.1017/jfm.2021.2.

[8] Breugem, W. P., Boersma, B. J., and Uittenbogaard, R. E., "The influence of wall permeability on turbulent channel flow," *Journal of Fluid Mechanics*, Vol. 562, 2006, p. 35–72. https://doi.org/10.1017/S0022112006000887.

[9] Rosti, M. E., Cortelezzi, L., and Quadrio, M., "Direct numerical simulation of turbulent channel flow over porous walls," *Journal of Fluid Mechanics*, Vol. 784, 2015, p. 396–442. https://doi.org/10.1017/jfm.2015.566.

[10] Kuwata, Y., and Suga, K., "Direct numerical simulation of turbulence over anisotropic porous media," *Journal of Fluid Mechanics*, Vol. 831, 2017, p. 41–71. https://doi.org/10.1017/jfm.2017.619.

[11] Gómez-de Segura, G., and García-Mayoral, R., "Turbulent drag reduction by anisotropic permeable substrates – analysis and direct numerical simulations," *Journal of Fluid Mechanics*, Vol. 875, 2019, p. 124–172. https://doi.org/10.1017/jfm.2019.482.

[12] Choi, H., Moin, P., and Kim, J., "Active turbulence control for drag reduction in wall-bounded flows," *Journal of Fluid Mechanics*, Vol. 262, 1994, p. 75–110. https://doi.org/10.1017/S0022112094000431.

[13] Luhar, M., Sharma, A. S., and McKeon, B. J., "Opposition control within the resolvent analysis framework," *Journal of Fluid Mechanics*, Vol. 749, 2014, p. 597–626. https://doi.org/10.1017/jfm.2014.209.

[14] Ibrahim, J. I., Guseva, A., and Garcia-Mayoral, R., "Selective opposition-like control of large-scale structures in wall-bounded turbulence," *Journal of Physics: Conference Series*, Vol. 1522, No. 1, 2020, p. 012015. https://doi.org/10.1088/1742-6596/1522/1/012015.

[15] Yao, J., and Hussain, F., "Drag reduction via opposition control in a compressible turbulent channel," *Phys. Rev. Fluids*, Vol. 6, 2021, p. 114602. https://doi.org/10.1103/PhysRevFluids.6.114602.

[16] Bewley, T. R., Moin, P., and Temam, R., "DNS-based predictive control of turbulence: an optimal benchmark for feedback algorithms," *Journal of Fluid Mechanics*, Vol. 447, 2001, p. 179–225. https://doi.org/10.1017/S0022112001005821.

[17] Jung, W. J., Mangiavacchi, N., and Akhavan, R., "Suppression of turbulence in wall-bounded flows by high-frequency spanwise oscillations," *Physics of Fluids A: Fluid Dynamics*, Vol. 4, No. 8, 1992, pp. 1605–1607. https://doi.org/10.1063/1.858381.

[18] Choi, J.-I., Xu, C.-X., and Sung, H. J., "Drag Reduction by Spanwise Wall Oscillation in Wall-Bounded Turbulent Flows," *AIAA Journal*, Vol. 40, No. 5, 2002, pp. 842–850. https://doi.org/10.2514/2.1750.

[19] Quadrio, M., and Ricco, P., "Critical assessment of turbulent drag reduction through spanwise wall oscillations," *Journal of Fluid Mechanics*, Vol. 521, 2004, p. 251–271. https://doi.org/10.1017/S0022112004001855.

[20] Gatti, D., and Quadrio, M., "Reynolds-number dependence of turbulent skin-friction drag reduction induced by spanwise forcing," *Journal of Fluid Mechanics*, Vol. 802, 2016, p. 553–582. https://doi.org/10.1017/jfm.2016.485.

[21] Rouhi, A., Fu, M., Chandran, D., Zampiron, A., Smits, A., and Marusic, I., "Turbulent drag reduction by spanwise wall forcing. Part 1. Large-eddy simulations," *Journal of Fluid Mechanics*, Vol. 968, 2023, p. A6. https://doi.org/10.1017/jfm.2023.499.

[22] Quadrio, M., Ricco, P., and Viotti, C., "Streamwise-travelling waves of spanwise wall velocity for turbulent drag reduction," *Journal of Fluid Mechanics*, Vol. 627, 2009, p. 161–178. https://doi.org/10.1017/S0022112009006077.

[23] Yao, J., and Hussain, F., "Supersonic turbulent boundary layer drag control using spanwise wall oscillation," *Journal of Fluid Mechanics*, Vol. 880, 2019, p. 388–429. https://doi.org/10.1017/jfm.2019.727.

[24] Quadrio, M., Floryan, J. M., and Luchini, P., "Effect of streamwise-periodic wall transpiration on turbulent friction drag," *Journal of Fluid Mechanics*, Vol. 576, 2007, p. 425–444. https://doi.org/10.1017/S0022112007004727.

[25] Gómez, F., Blackburn, H. M., Rudman, M., Sharma, A. S., and McKeon, B. J., "Streamwise-varying steady transpiration control in turbulent pipe flow," *Journal of Fluid Mechanics*, Vol. 796, 2016, p. 588–616. https://doi.org/10.1017/jfm.2016.279.

[26] Moarref, R., and Jovanović, M. R., "Controlling the onset of turbulence by streamwise travelling waves. Part 1. Receptivity analysis," *Journal of Fluid Mechanics*, Vol. 663, 2010, p. 70–99. https://doi.org/10.1017/S0022112010003393.

[27] Lieu, B. K., Moarref, R., and Jovanović, M. R., "Controlling the onset of turbulence by streamwise travelling waves. Part 2. Direct numerical simulation," *Journal of Fluid Mechanics*, Vol. 663, 2010, p. 100–119. https://doi.org/10.1017/S002211201000340X.

[28] Cheng, X., Qiao, Z., Zhang, X., Quadrio, M., and Zhou, Y., "Skin-friction reduction using periodic blowing through streamwise slits," *Journal of Fluid Mechanics*, Vol. 920, 2021, p. A50. https://doi.org/10.1017/jfm.2021.439.

[29] Hussein, M. I., Biringen, S., Bilal, O. R., and Kucala, A., "Flow stabilization by subsurface phonons," *Proceedings of the Royal Society A: Mathematical, Physical and Engineering Sciences*, Vol. 471, No. 2177, 2015, p. 20140928. https://doi.org/10.1098/rspa.2014.0928, URL https://royalsocietypublishing.org/doi/abs/10.1098/rspa.2014.0928.

[30] Orlandi, P., *Fluid flow phenomena: a numerical toolkit*, Vol. 55, Springer Science & Business Media, 2000.

[31] Kim, J., and Moin, P., "Application of a fractional-step method to incompressible Navier-Stokes equations," *Journal of Computational Physics*, Vol. 59, No. 2, 1985, pp. 308–323. https://doi.org/https://doi.org/10.1016/0021-9991(85)90148-2.

[32] Wray, A. A., "Minimal storage time advancement schemes for spectral methods," *NASA Ames Research Center, California, Report No. MS*, Vol. 202, 1990.

[33] Bae, H. J., Lozano-Durán, A., Bose, S. T., and Moin, P., "Turbulence intensities in large-eddy simulation of wall-bounded flows," *Phys. Rev. Fluids*, Vol. 3, 2018, p. 014610. https://doi.org/10.1103/PhysRevFluids.3.014610.

13

[34] Bae, H. J., Lozano-Durán, A., Bose, S. T., and Moin, P., "Dynamic slip wall model for large-eddy simulation," *Journal of Fluid Mechanics*, Vol. 859, 2019, p. 400–432. https://doi.org/10.1017/jfm.2018.838.

[35] Lozano-Duran, A., and Bae, H. J., "Turbulent channel with slip boundaries as a benchmark for subgrid-scale models in LES," *Annual research briefs. Center for Turbulence Research*, Vol. 2016, 2016, pp. 97–103.

[36] Jiménez, J., and Moin, P., "The minimal flow unit in near-wall turbulence," *Journal of Fluid Mechanics*, Vol. 225, 1991, p. 213–240. https://doi.org/10.1017/S0022112091002033.

[37] Chung, D., Chan, L., MacDonald, M., Hutchins, N., and Ooi, A., "A fast direct numerical simulation method for characterising hydraulic roughness," *Journal of Fluid Mechanics*, Vol. 773, 2015, p. 418–431. https://doi.org/10.1017/jfm.2015.230.

[38] Jiménez, J., "Coherent structures in wall-bounded turbulence," *Journal of Fluid Mechanics*, Vol. 842, 2018, p. P1. https://doi.org/10.1017/jfm.2018.144.